Front. Environ. Sci. Eng. 2023, 17(9): 109
https://doi.org/10.1007/s11783-023-1709-x

RESEARCH ARTICLE

Self-sustained catalytic combustion of CO enhanced by micro fluidized bed: stability operation, fluidization state and CFD simulation

Zirui Zhang[1,2], Chenhang Zhang[1], Huan Liu[1], Feng Bin (✉)[1], Xiaolin Wei[1], Running Kang[1], Shaohua Wu (✉)[3], Wenming Yang[4], Hongpeng Xu (✉)[5]

1 State Key Laboratory of High-Temperature Gas Dynamics, Institute of Mechanics, Chinese Academy of Sciences, Beijing 100190, China
2 School of Engineering Science, University of Chinese Academy of Sciences, Beijing 100049, China
3 School of Energy and Power Engineering, Dalian University of Technology, Dalian 116000, China
4 Department of Mechanical Engineering, National University of Singapore, Singapore 117575, Singapore
5 School of Vehicle and Energy, Yanshan University, Qinhuangdao 066000, China

HIGHLIGHTS

- Catalytic combustion in fluidized bed realizes efficient heat and mass transfer.
- Catalytic combustion in fluidized bed reduces the lean combustion limits.
- Catalytic combustion and flame combustion can be coupled.
- The diffusion/kinetics limited reaction model is suitable for catalytic combustion.

ARTICLE INFO

Article history:
Received 10 December 2022
Revised 3 March 2023
Accepted 6 March 2023
Available online 1 April 2023

Keywords:
Self-sustained catalytic combustion
Carbon monoxide
$Cu_{1-x}Ce_xO_y$
Fluidized bed
Computational fluid dynamics

GRAPHIC ABSTRACT

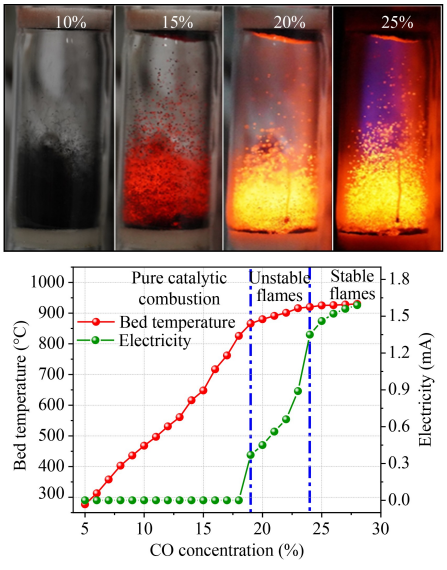

ABSTRACT

A micro fluidized bed reactor was used to study the self-sustaining catalytic combustion of carbon monoxide (CO). The $Cu_{1-x}Ce_xO_y$ catalyst, as well as the pure CuO and CeO_2, are used to investigate the contributing mechanism of different active sites including dispersed CuO and Cu–Ce solid solutions. The ignition temperature (T_i) of CO over these catalysts at a flow rate of 2000 mL/min followed the order: 74 °C ($Cu_{0.5}Ce_{0.5}O_y$) < 75 °C ($Cu_{0.25}Ce_{0.75}O_y$) < 84 °C ($Cu_{0.75}Ce_{0.25}O_y$) < 105 °C (CuO) < 500 °C (CeO_2). Furthermore, the lean combustion limits (equivalence ratio ϕ) over these catalysts under the flow rates of 750–3000 mL/min (through fixed, bubbling, and fluidized bed) were also measured, which are $Cu_{0.5}Ce_{0.5}O_y$ < $Cu_{0.25}Ce_{0.75}O_y$ < $Cu_{0.75}Ce_{0.25}O_y$ < CuO < CeO_2. The fluidized bed was simulated using the Eulerian two-fluid model (TFM) coupled with a diffusion/kinetic-limited reaction model to evaluate the influence of operation conditions on the self-sustained combustion of CO. The predicted maximum temperature agreed with the experimental measurements, demonstrating the validity of the kinetic model and simulation parameters. The results of catalytic combustion with

✉ Corresponding authors
E-mails: binfeng@imech.ac.cn (F. Bin); wushaohua@dlut.edu.cn (S. Wu); xuhongpeng@ysu.edu.cn (H. Xu)

increasing CO concentrations suggest that the catalytic combustion reaction could co-exist with the flamed combustion. When a high concentration of CO is used, a blue-purple flame caused by CO combustion appears in the upper part of the fluidized bed, indicating that the range of CO-containing exhaust gas purification could be expanded to a larger range using the fluidized-bed catalytic combustion technique.

1 Introduction

The off-gas emitted by the steel manufacturing industry contains a large amount of CO which is a promising fuel candidate. However, the emitted CO/O_2 mixture is potentially highly flammable. As a result, the mixture is typically post-processed in the methane combustion-supported flare burners before being released into the atmosphere, resulting in massive energy waste. To recover the wasted heat, we recently proposed a CO self-sustained catalytic combustion technique in which the CO/O_2 mixture is firstly catalyzed to generate some local high-temperature spots at the catalyst surface. These hot spots then dissociate the adjacent CO and O_2 molecules, leading to a thermochemical runaway followed by a rapid transition to self-sustained intense combustion (Kang et al., 2021). This novel technique allows for flameless combustion with considerably lower ignition temperatures than the direct flame combustion approach. Furthermore, it aids in diluting the CO/air mixture, thereby avoiding unwanted explosions (Bin et al., 2015).

Currently, both fixed and fluidized bed reactors are widely used in catalytic reactions (Iamarino et al., 2002; Rau et al., 2010; Yang et al., 2014; Parmon et al., 2015; Goshima et al., 2017; Paasikallio et al., 2017; Liu et al., 2020a; Dubinin et al., 2021; Liang et al., 2022). Typical catalysts are Cu−Ce mixed oxides with solid solution structures, which are the most active CO oxidation media in non-precious metal materials (Zhang et al., 2018). Chen et al. (2019) demonstrated using a fixed bed reactor that the catalytic reaction occurs at the copper–ceria interfacial perimeter via a site cooperation mechanism: the Cu^{+}−$[O_v]$−Ce^{3+} site chemically adsorbs CO, which reacts with nearby dissociative lattice oxygen. According to Du et al. (2016), the maximum CO-catalytic activity is achieved when the concentration of copper in the solid solution of copper-cerium reaches 30% when considering the maximum copper dispersion. Bin et al. (2019) investigated the steady ignition limit of copper-cerium solid solution in a fixed bed reactor at varying gas flow rates. Kang et al. (2020) developed a bistable kinetic reaction model based on CO-catalytic ignition that accounts for the transition from low to high steady-state reactivity. Unfortunately, the fixed bed reactor has hot spots which are caused by the exothermic reactions, resulting in the sintering and agglomeration of active nanoparticles of catalysts (Duyar et al., 2015). Additionally, carbon deposition is always found at the outlet of the fixed bed due to the lack of gaseous oxygen at that location.

Compared with fixed bed reactors, fluidized bed reactors (Wang et al., 2013; Bizon, 2016; Li et al., 2017) exhibit a higher degree of uniform temperature distribution, higher heat transfer rate, better adequate gas-solid contact (Li et al., 2021), less agglomeration (Nam et al., 2021), and suppression of external diffusion, resulting better catalysis performance. Jia et al. (2020) discovered that CO_2 methanation in fluidized bed results in higher rates and product content than in a fixed bed. Liu and Ji (2013) confirmed that abundant active sites on the used catalyst surfaces were exposed in a fluidized bed with a tubular fiber structure, compared with the dense accumulation distribution in a fixed bed. Żukowski and Berkowicz (2019a) testified that changing the fluidized bed from non-catalytic to catalytic mode increased the conversion of outlet polypropylene from 57% to 85%. However, no statistical data relating to the CO catalytic combustion caused by fluidized bed, particularly when maintained at the self-sustaining stage, has been reported so far.

The current study first determines the relationship between the fluidization structure and the catalytic combustion performance in terms of ignition temperature, conversion efficiency, lean burn limit, and temperature distribution using $Cu_xCe_{1-x}O_y$ as the catalyst. Then, under self-sustaining combustion conditions, a CFD study is carried out in which a diffusion reaction model is employed to investigate the effects of operating parameters on the spatial distributions of temperature, velocity, and species concentrations in the reactor. The results of this study not only provide fundamental knowledge of CO catalytic combustion in fluidized bed reactors but also hint at a method for better utilization of CO in steelmaking exhaust.

2 Experimental

2.1 Preparation of the catalysts

In a molar ratio of 1:1, AR copper nitrate (Wencheng, Shanxi, China) and AR cerous nitrate (Wencheng, Shanxi, China) were dissolved completely in ethyl alcohol at 80 °C. For pore formation, oxalic acid was quickly added to the aforementioned nitrate. The gel was aged for 48 h at room temperature, then excess water was removed at 105 °C before being calcined in air at 550 °C for 4 h. The catalysts obtained were labeled as $Cu_{0.5}Ce_{0.5}O_y$. The same procedure was used to prepare CuO, CeO_2, $Cu_{0.25}Ce_{0.75}O_y$, and $Cu_{0.75}Ce_{0.25}O_y$ catalysts.

2.2 Characterization

The x-ray diffraction analysis of the sample crystal structure was performed using a Philips X'Pert diffractometer (Netherlands). Raman spectra were collected using a HORIBA LabRAM HR Evolution (China) which uses a 488 nm laser as an excitation source. The Kratos Axis Ultra DLD spectrometer (UK) was used to acquire the X-ray photoelectron spectroscopy (XPS). In the temperature-programmed reduction of H_2 (H_2-TPR), the rate of heating was 10 °C/min to 800 °C on a TP5080B chemisorption analyzer (China). In an examination of temperature-programmed desorption of CO (CO-TPD-MS), 5% of CO was delivered at a rate of 100 mL/min to the reactor. Adsorption of CO at 20 °C for 30 minutes was followed by exposure to Helium. The reactor was heated to 1000 °C (10 °C/min), and the desorption signals were measured using a Pfeiffer PrismaPlus mass spectrometer (Germany). All samples were protected with pure argon before all characterization tests to isolate the 550 °C air to prevent the unpredictable effects of water and oxygen in the air.

2.3 CO self-sustained catalytic combustion

The main component of the test stand was the micro fluidized bed reactor which included a quartz tube (20 mm in diameter), a temperature-controlled heating furnace, and four mass flow controllers to regulate the flow of CO, O_2, and N_2. The catalyst dosage was 1000 mg with the particle size measuring 0.2–0.3 mm. The carbon monoxide catalytic ignition experiment was carried out under the constant heating condition (5 °C/min) starting at 25 °C. There were two K-type thermocouples used: one between the reactor and the furnace to regulate the furnace temperature, and another placed into the catalyst to monitor the bed temperature. The temperature distribution of the reactor surface was measured using Infrared cameras (FLIRT640, USA). The outflow of CO, O_2, and CO_2 was monitored using an online Maihak FTIR system (QGS-08, Germany). To prevent the influence of delay on the experiment, we evaluated the delay time of different flow rates: 1000 mL/min (3.5 s), 2000 mL/min (3.0 s), and 3000 mL/min (2.8 s). After subtracting the delay time from the concentration-time data, the new temperature-concentration data was generated by combining it with the temperature-time data, therefore, avoiding the influence of the delay time on the accuracy of the experiment.

3 Results and discussion

3.1 XRD, Raman and XPS analysis of catalysts

The XRD spectra of $Cu_xCe_{1-x}O_y$ catalysts are shown in Fig. 1(a). All cerium-based catalysts displayed characteristic diffraction peaks corresponding to fluorite-type oxide structure of CeO_2 structures (JCPDS 34-0394), and the peaks at 28.5°, 33.1°, 47.6°, and 56.3° corresponded to the crystal planes of (111), (200), (220), and (311), respectively (Zou et al., 2006; Hu et al., 2009; Jia et al., 2012). The diffraction peaks of $Cu_{0.25}Ce_{0.75}O_y$, $Cu_{0.5}Ce_{0.5}O_y$, and $Cu_{0.75}Ce_{0.25}O_y$ were broader and shifted to a higher 2θ direction than those of pure CeO_2, indicating that some copper ions entered the CeO_2 lattice to form Cu-Ce solid solution. Two diffraction peaks in CuO at 35.5° and 38.9° can be attributed to (–111) or (111) planes in the monoclinic crystal structure (JCPDS 45-0937). As shown in the XRD patterns for $Cu_{0.5}Ce_{0.5}O_y$ and $Cu_{0.75}Ce_{0.25}O_y$, which correspond to crystallite sizes (determined by Scherrer equation) of 35.6 and 69.0 nm, respectively, such two peaks, which are not observed in the XRD pattern for $Cu_{0.25}Ce_{0.75}O_y$, begin to appear and exhibit a gradual enhancement with an increase in copper content in the catalysts. The absence of a CuO phase in XRD patterns arises from uniformly distributed copper species and finely dispersed clusters on cerium oxide (Águila et al., 2008; Zeng et al., 2013). The presence of monoclinic copper oxide phases is corroborated by the Raman spectra (Fig. 1(b)) of CuO at 281, 332, and 623 cm^{-1} A_{1g}, B_{1g}, and B_{2g} modes, respectively, which are less easily detected from $Cu_xCe_{1-x}O_y$ as cerium concentration increases. CeO_2 displays a prominent band at 453 cm^{-1} associated with the F_{2g} symmetric vibrational mode of the cubic fluorite structure, while the low peak at 1172 cm^{-1} is due to primary A_{1g} asymmetry. The F_{2g} peak shifts towards lower wave numbers as copper concentration decreases, indicating the generation of oxygen vacancies in $Cu_xCe_{1-x}O_y$ catalysts. The highest content of oxygen vacancies is associated with the maximum offset for $Cu_{0.5}Ce_{0.5}O_y$ (Liu et al., 2020b).

The XPS analysis provides evidence for the valences of surficial copper and cerium of catalysts (Avgouropoulos

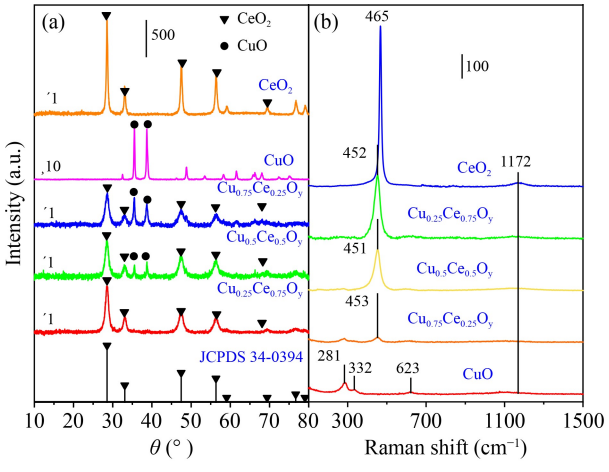

Fig. 1 X-ray diffractogram (a) and average Raman spectra (b) of catalysts.

and Ioannides, 2003). As shown in Fig. 2, the Cu $2p_{3/2}$ area is adequately fitted as two contributions: a main one at 932.1 eV (Cu^{+}) and another one at 933.7 eV (Cu^{2+}) with satellite lines at 945–940 eV. Spectra observed in the Ce 3d region for the bulk CeO_2 and $Cu_xCe_{1-x}O_y$ can be fitted with eight peaks identified as V (882.6 eV), V_2 (888.4 eV), and V_3 (898.5 eV) attributed to the $3d_{5/2}$, whereas U (900.9 eV), U_2 (907.5 eV), and U_3 (916.7 eV), ascribed to the $3d_{3/2}$ of Ce^{4+} state. Besides, the peaks V_1 (885.2 eV) appear in the $3d_{5/2}$, whereas U_1 (902.5 eV) appears in the $3d_{3/2}$ of the Ce^{3+} state (Wang et al., 2015; Wang et al., 2021; Talluri et al., 2022). The appearance of Ce^{3+} leads to the formation of oxygen vacancies in the catalysts which trigger oxygen release/storage between Ce^{3+} and Ce^{4+}.

The relative proportion of Cu^{+}/Cu is derived by dividing the area of the Cu^{+} peak by the total area of Cu^{+} and Cu^{2+} peaks, whereas the proportion of Ce^{3+}/Ce is calculated by dividing the area of the two Ce^{3+} peaks by the overall region of Ce^{3+} and Ce^{4+} regions. According to the valence distribution of Cu and Ce (Table 1), the proportions of Cu^{+}/Cu and Ce^{3+}/Ce exhibit a "roller coaster" tendency with increasing copper and cerium content. The maximum Cu^{+}/Cu and Ce^{3+}/Ce proportions found in $Cu_{0.5}Ce_{0.5}O_y$ correspond to 0.620 and 0.217, respectively. As a result, when combined with the formation of oxygen vacancies measured by Raman spectra, these Cu^{+} and Ce^{3+} species could be produced concurrently as Cu^{+}–[O_v]–Ce^{3+} ([O_v] implies lattice oxygen) via the formation of Ce^{3+} by reduction of Ce^{4+}, located at the interface of copper-cerium phase (Avgouropoulos et al., 2005; Gu et al., 2018; Zhao et al., 2019; Meng et al., 2021).

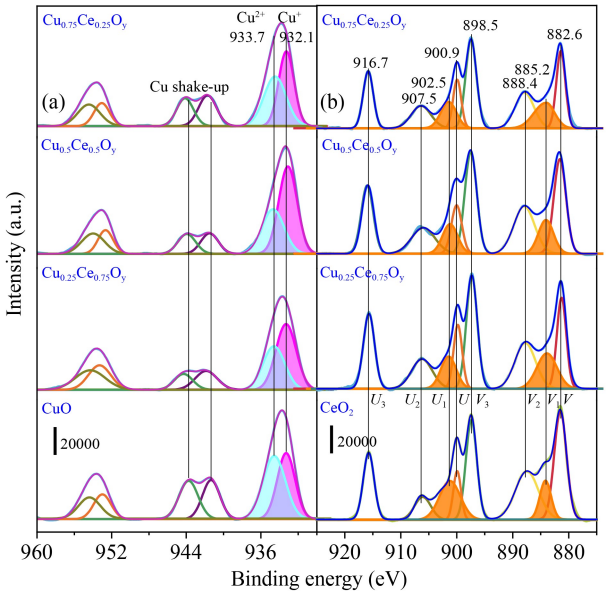

Fig. 2 X-ray photoelectron spectra of the catalysts in the Cu 2p (a) and Ce 3d (b).

3.2 Temperature-programmed analysis

The redox behavior of catalysts is highlighted by H_2-TPR measurement (Fig. 3(a)). At temperatures over 200 °C, a slight reduction of bulk CeO_2 is observed due to its poor reduction properties. The kinetic profiles of $Cu_xCe_{1-x}O_y$ series, such as $Cu_{0.25}Ce_{0.75}O_y$, are characterized by three reduction peaks: α peak (154 °C), generated by the reduction of Cu in Cu-Ce solid solution; β peak (169 °C), associated with dispersed CuO_x clusters; and γ peak (195 °C), related to crystallize CuO (Luo et al., 2005). By contrast, the TPR profile of $Cu_{0.5}Ce_{0.5}O_y$ shows a shift of the reduction peaks towards the lower temperature direction. Furthermore, both the α and β peaks exhibit significant growth while the γ peak shows a declining trend, reflecting a rise in copper species in the solid solution phase and amorphous CuO_x clusters as a result of increased copper loading and dispersion. As the copper loading is increased further, a relatively broad area of reduction is observed as shown in the TPR files for $Cu_{0.75}Ce_{0.25}O_y$, which proceeds uninterruptedly from 120 to 250 °C. This indicates that the reduction peaks are returning towards the higher temperature direction when compared with the peaks for $Cu_{0.5}Ce_{0.5}O_y$. Then only β and γ peaks exist in the CuO owing to the absence of cerium (Chen et al., 2013). Although the H_2 consumption of catalysts increases with copper loading (Table 1), the conclusion that redox properties of catalysts are primarily affected by the reduction temperature and the uptake of α peak rather than the total H_2 consumption during H_2-TPR exhibits a high turnover frequency (TOF). This indicates that H_2 consumption is no longer dominant, which will be

Table 1 The surface elemental valence distribution and the H_2/CO consumption of catalysts during H_2-TPR and CO-TPD test

Catalyst	Surface atomic ratio		H_2 consumption (μmol/g)				CO consumption (μmol/g)			
	Cu^{+}/Cu	Ce^{3+}/Ce	α	β	γ	Total	α	β	γ	Total
CeO_2	–	0.12	0	0	0	0	0	0	5.9	5.9
$Cu_{0.25}Ce_{0.75}O_y$	0.51	0.20	16.4	15.6	71.5	103.5	29.8	22.3	8.7	60.8
$Cu_{0.5}Ce_{0.5}O_y$	0.62	0.22	57.1	61.9	18.4	137.4	54.5	42.8	0	97.3
$Cu_{0.75}Ce_{0.25}O_y$	0.50	0.20	27.7	107.1	25.0	159.8	27.6	16.6	5.7	49.9
CuO	0.43	–	0	100.8	64.1	164.9	0	4.5	0	4.5

confirmed by activity test results in the following paper. The redox properties of these catalysts follow the sequence: $Cu_{0.5}Ce_{0.5}O_y$ > $Cu_{0.25}Ce_{0.75}O_y$ > $Cu_{0.75}Ce_{0.25}O_y$ > CuO > CeO_2.

CO-TPD (Fig. 3(b)) is used as a rate-determining step (RDS) of CO oxidation to characterize the surface oxygen functional groups of catalysts. Because intermediate species are weakly stable at low temperatures, the minimum desorbed temperature during CO-TPD could also be an indicator of increased activity. When heated, almost all the CO molecules adsorbed on the catalyst will be released as gaseous CO_2. Combined with step-response runs, such a phenomenon has been confirmed by our previous works that the adsorbed CO reacts with lattice oxygen, following the M-K mechanism (Kang et al., 2020). During TPD, only minute quantities of CO_2 are found in relation to CeO_2 at 255 °C. Similarly, CuO has a small peak for CO_2 at 140 °C. Unlike the faint activity of CuO and CeO_2, the $Cu_xCe_{1-x}O_y$ catalysts induce immediate desorption of CO once the temperature ramp is initiated. The CO_2 profiles are distinguished by a major peak (α peak) at about 90 °C, a second peak above 150 °C (β peak), and a third peak (only exists for $Cu_{0.25}Ce_{0.75}O_y$ and $Cu_{0.75}Ce_{0.25}O_y$) at approximately 255 °C (γ peak). Our previous work established that the α and β carbonyls peaks correspond to CO adsorbed on the Cu−Ce solid solutions (Cu^+−[CO]−Ce^{3+}) and Cu^+ ions of CuO (Cu^+−CO), while the γ peak is attributed to CO adsorbed on the Ce^{3+} ions to form carbonates (Kang et al., 2020). The desorbed quantities of CO in Table 1 illustrate that the equivalent copper incorporated into cerium enhances the dispersion of catalysts and the formation of Cu−Ce solid solutions. This behavior leads to twice the adsorption capacity of CO for Cu^+−[CO]−Ce^{3+} and Cu^+ ions and induces a shift of both α and β peaks towards the low temperature directly.

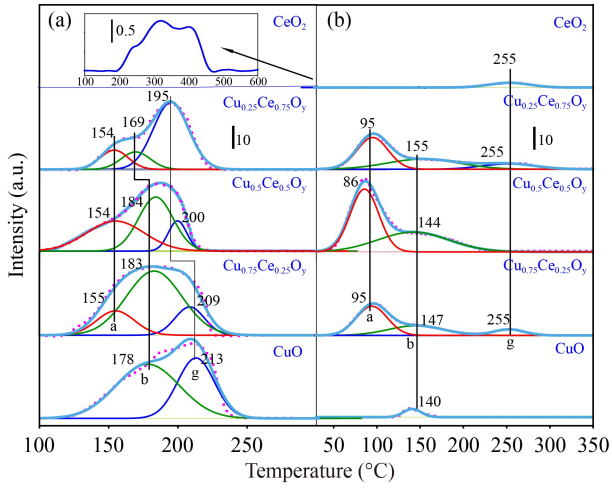

Fig. 3 H_2-temperature-programmed reduction (a) and CO-temperature-programmed desorption (b) profiles of catalysts.

3.3 CO catalytic ignition experiment

The CO conversions over the catalysts during the heating and cooling operation are depicted in Fig. 4. Consider the CuO, which has three major phases in the heating feed condition: The first stage is an induction process with a slow transition from 90 to 105 °C; the second stage is the ignition process which occurs at the catalyst surface under a transient state (105–110 °C); and the final stage is the temperature zone (above the ignition temperature, > 110 °C) where the CO conversion reaches its maximum. The catalytic reactivity of the CO ignition process, which is negatively correlated with the ignition temperature (T_i, the temperature at which CO conversion reaches 30%), follows the order: $Cu_{0.5}Ce_{0.5}O_y$ (74 °C) >$Cu_{0.25}Ce_{0.75}O_y$ (75 °C) > $Cu_{0.75}Ce_{0.25}O_y$ (84 °C) > CuO (105 °C) > CeO_2 (500 °C). It should be noted that for the inactive CeO_2, 5% content of CO fails to achieve self-sustaining combustion. Furthermore, as compared to the heating curve, the cooling curve of CO conversion changes towards the low temperature direction. This hysteresis, caused by the exothermic effect of CO combustion on the catalyst bed and heat buildup, allows the control temperature to drop below the ignition temperature without altering the reaction rate.

3.4 Determination of minimum fluidization and bubbling flow rate

To investigate the influence of fluidization states on CO self-sustained catalytic combustion, the minimum fluidization and bubble flow rates should be determined. The minimum fluidization flow rate Q_{mf} is often defined as the rate at which the pressure drop line of the fixed bed intersects with the horizontal line of the whole fluidized bed. When Q is increased to fluidize the particles, the ΔP curve measured in the Q-ascending run shifts to higher

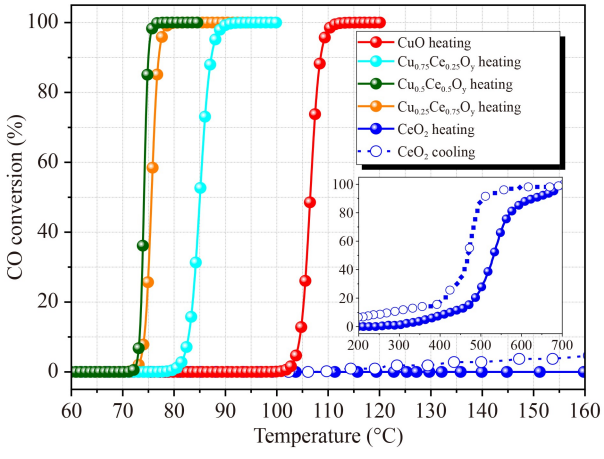

Fig. 4 Ignition curves of CO and the temperature fields in micro-fluidized bed reactor under 5% CO/air atmosphere and 2000 mL/min flow rate.

values than theΔP curve measured in the Q-descending run. This phenomenon is attributed to the different compactness degree of initial filling in the particle bed and the need to overcome the additional adhesion force among the catalyst particles. Therefore, as shown in curve b of Fig. 5, the Q_{mf} in the Q-descending run may be determined using Richardson's classical method (Benyahia, 1994; Żukowski and Berkowicz, 2019b). The minimum bubble flow rate Q_{mb} is generally assessed with the naked eye, but in micro fluidized beds, this approach is difficult to estimate. According to Liu et al. (2008), the standard deviation σ_P derived from pressure fluctuations increased significantly with bubble formation. Thus, Q_{mb} is defined as the point at which σ_P begins to increase continuously and rapidly as Q increases.

3.5 CO self-sustained catalytic combustion experiment

Fig. 6 depicts the equivalence ratio (ϕ) limit and the corresponding bed temperature profile for CO self-sustained combustion under lean CO conditions. In this case, ϕ is defined as the ratio of CO to oxygen in the inlet gas divided by the oxygen required for the complete combustion of CO. As expected, $Cu_{0.5}Ce_{0.5}O_y$ performs the best among the $Cu_xCe_{1-x}O_y$ catalysts, with the lowest lean stability limit found, followed by $Cu_{0.25}Ce_{0.75}O_y$ and then $Cu_{0.75}Ce_{0.25}O_y$. The $Cu_xCe_{1-x}O_y$ catalysts exhibit a lean limit with a local minimum value of about 1000 mL/min (bubbling bed stage), after which the values slightly increase with the fluidization (flow rate). The quantity of CO is insufficient to achieve self-sustained combustion at low flow rates. At the same limit, increased gas flow rates may blow away hot patches on the catalyst surface due to heat loss. Because the particles are in a fluidized state, this phenomenon is not as pronounced as it is in fixed beds. However, for CuO and CeO_2 (Fig. 6(a)), the ϕ values decrease gradually with flow rate since the heat received by the gas stream from the surface of catalyst particles at high temperatures is overcome by the heat generated from CO combustion, particularly for CeO_2. However, there is a limit to such a decreasing tendency

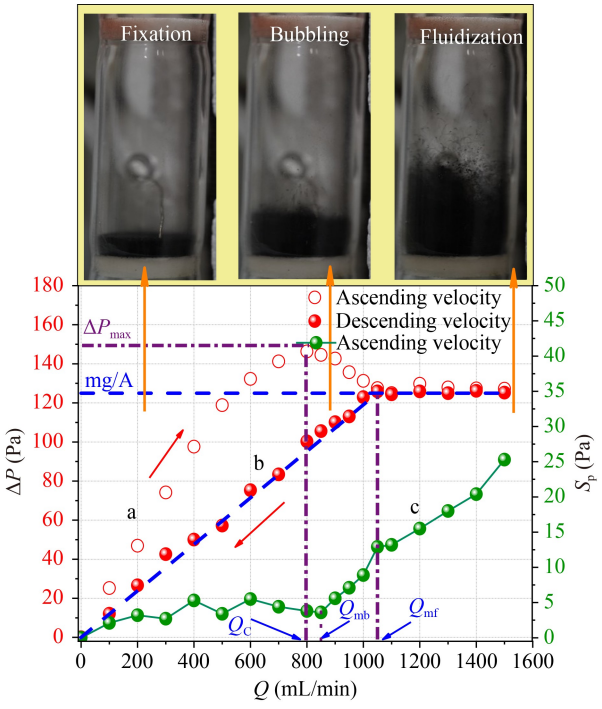

Fig. 5 Determination of Q_{mf}, Q_{mb} and ΔP_{max} in a typical operation (Dt =20 mm, dp =0.2–0.3 mm and Hs =100 mm).

which is considered as the convergence ϕ of 0.07 between the curves of CuO and $Cu_{0.75}Ce_{0.25}O_y$. Fig. 6(b) shows the bed temperature at the flow rate associated with a steady combustion limit. Except for CuO, where the minimum bed temperature was reached at a flow rate of 1000 mL/min, the bed temperature increases as the flow rate increases for other catalysts. Fig. 6(c) shows the spatial temperature distributions of CeO_2, $Cu_{0.5}Ce_{0.5}O_y$, and CuO for the micro-fluidized bed when the self-sustained combustion runs at the lean limit corresponding to the 3000 mL/min flow rate. The high temperature zone is detected below the middle of the micro-fluidized bed, and the upper quartz bed has a higher temperature than the bed wall since it receives more convective and radiative heat transfer from the high temperature gases. Particularly, the

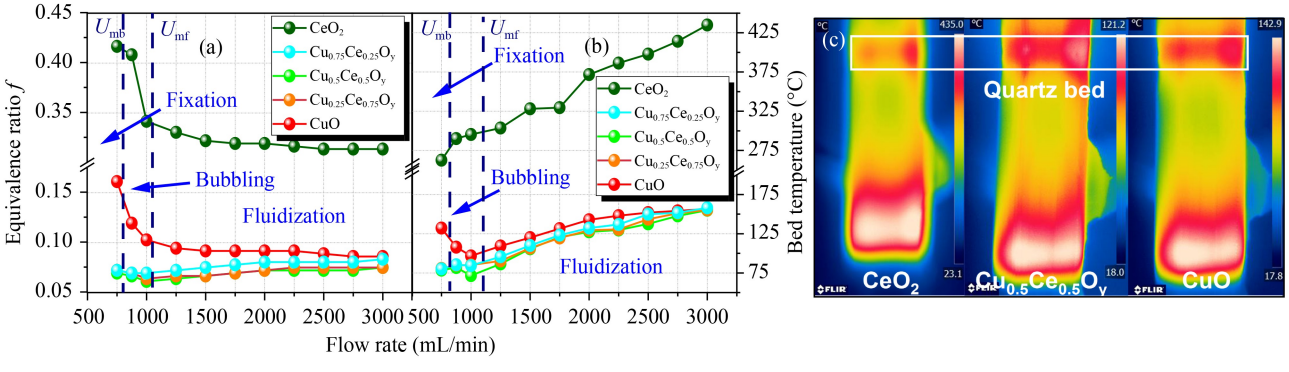

Fig. 6 Lean limits of CO self-sustained combustion (a), corresponding bed axial (b) and wall (c) temperatures.

right wall is close to the electric furnace and dissipates less heat, thus being warmer than the left wall.

The temperature along the axial wall of the reactor (Fig. 7) is measured using the 2-D temperature field of CO self-sustained catalytic combustion (Fig. 6(c)). The corresponding ratios of each line are ascertained by the combustion limits shown in Fig. 6(a). Axial distance 0–8 mm for high temperature zone, corresponding to the height of catalysts in the fluidized state, and the highest temperature zone for each catalyst gradually shifted upward with the flow rate, because catalyst particles can be blown to a higher level with flow rate (Girimonte and Formisani, 2009). The maximum temperature zone in both spatial distributions of catalyst particles in the fluidized bed is consistent for all the catalysts tested. However, at the fluidized bed state (3000 mL/min), because the particles of all the catalysts tested belong to Geldart-B (Q_{mf} decreases with increasing temperature),

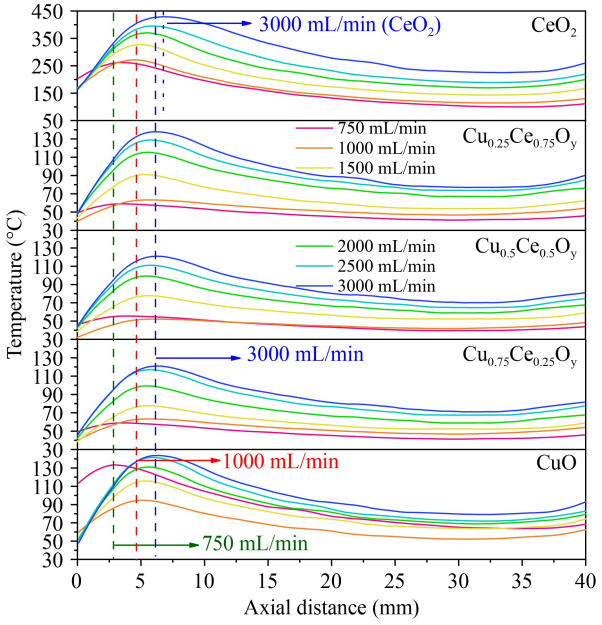

Fig. 7 Axial wall temperature along the combustion chamber.

the CO self-sustained combustion should run at the higher temperature zone than others over the inactive CeO_2, causing the CeO_2 particles blown to the higher positions.

3.6 Flame combustion induced by catalytic combustion

Fig. 8(a) shows the experimental setup: a pair of platinum electrode lines are placed parallel to the top middle of the fluidized bed forming a circuit with a 24-volt DC power source and an ammeter. The flow rate is set to 3000 mL/min, and the environment contains between 5% and 30% CO/Air. As shown in Figs. 8(b) and 8(c), as the CO concentration increased from 5% to 19%, the catalyst particles progressively transitioned from black to dark red and dazzling white, while the bed temperature rose from 266 to 866 °C. When the CO concentration increased above 19%, the rise in bed temperature began to slow. The clear flame pattern was difficult to capture with the naked eye, while the current expression bounced between 0 and extremely tiny values, indicating less stable flame combustion caused by catalytic combustion. When CO concentration exceeded 24%, the rise of bed temperature nearly stopped. The current expression steadied around a readable value, and a distinct columnar blue-purple flame could be observed in the upper part of the fluidized bed, suggesting that the flame was essentially stable. The flame generation may be explained by the upper limit of the migration rate of bulk phase lattice oxygen at high CO concentrations, while the heat generated by catalytic combustion is sufficient for the heat absorption reactions in the chain reaction of flame combustion (Lazarovici et al., 2004). It is worth noting that in the whole experiment, the CO conversion rate could reach 100%. Such a coupled combustion approach has a potential application background, and our future work will focus on it.

3.7 Numerical simulation of the self-sustained combustion

To validate the CO self-sustained catalytic combustion under different conditions, the gas-solid two-phase flow

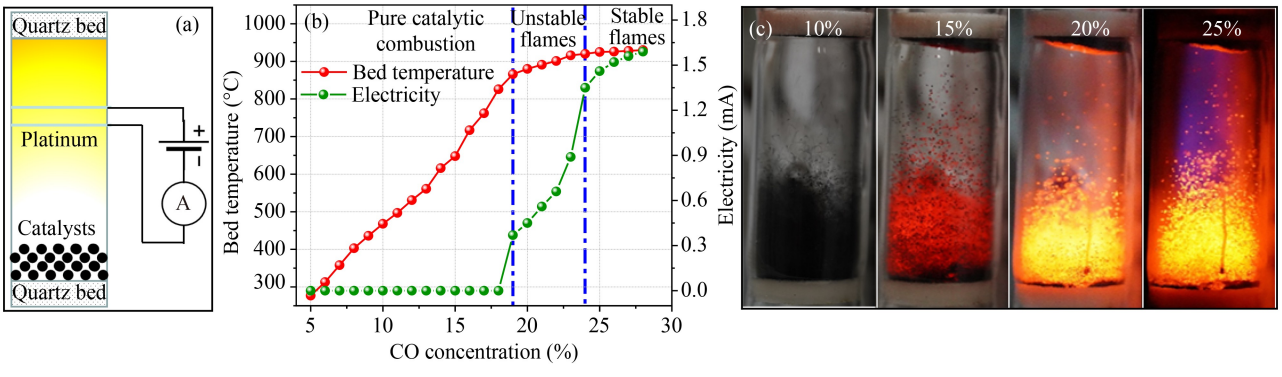

Fig. 8 Detection of induced flames at high CO concentration experimental sketch (a), bed temperatures and electricity (b), photograph of CO concentration of 10%, 15%, 20% and 25% (c).

in the fluidized bed is simulated by Ansys Fluent using the Eulerian two-fluid model (TFM). It considers 16000 cells that have been determined by the grid independence test for the 3-D simulation. The diffusion/kinetic-limited reaction model is also applied since the catalytic combustion follows the principle of heterogeneous reaction. As illustrated in Fig. 9, the numerical simulation is validated first. The radial line-average values of estimated temperatures along the axial direction of the reactor are utilized to compare with the experimental data from Fig. 7. Except for the reactor outlet, the calculated temperatures match the experimental measurements. The quartz has been heated up during self-sustained combustion (shown in Fig. 6), which can then heat the gas near the outlet. This is not considered in the simulation as a pure pressure outlet. Compared to the measured temperature, the high temperature zones from the simulation under different fluidization gas velocities are in similar positions. The errors between the measured peak temperatures and the predicted peak temperatures are within 5%, confirming the rationality of the kinetic model used in this simulation.

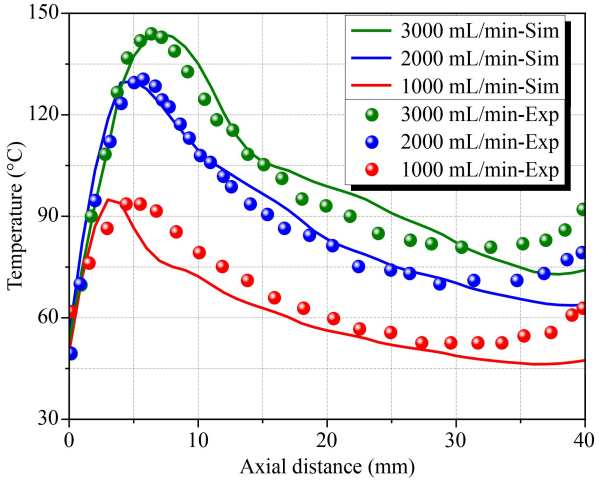

Fig. 9 Measured *vs.* simulated temperature along the axial direction of the reactor with $Cu_{0.5}Ce_{0.5}O_y$ being catalyst.

Fig. 10 shows the spatial distributions of the catalyst volume fraction, gas velocity, CO_2 concentration, and temperature under different fluidization gas flow rates. The fluidization becomes increasingly visible as the fluidization gas flow rate increases, resulting in an uneven flow field of gas. Moreover, the greater gas flow rate allows the gas to flow more easily through the bed materials, resulting in the CO self-sustained catalytic combustion occurring in multiple locations inside the reactor. This could enlarge the high temperature zone, increasing the probability of collecting the energy from low CO concentrations emitted gas. In this instance, additional heat may be recovered from the released gas.

4 Conclusions

Using a micro fluidized-bed reactor, the self-sustained catalytic combustion of CO was investigated over the $Cu_xCe_{1-x}O_y$ catalyst. $Cu_{0.5}Ce_{0.5}O_y$ has the lowest ignition temperature and the lowest lean ignition limit. The well-dispersed Cu–Ce solid solution structure is responsible for the remarkable reduction performance demonstrated

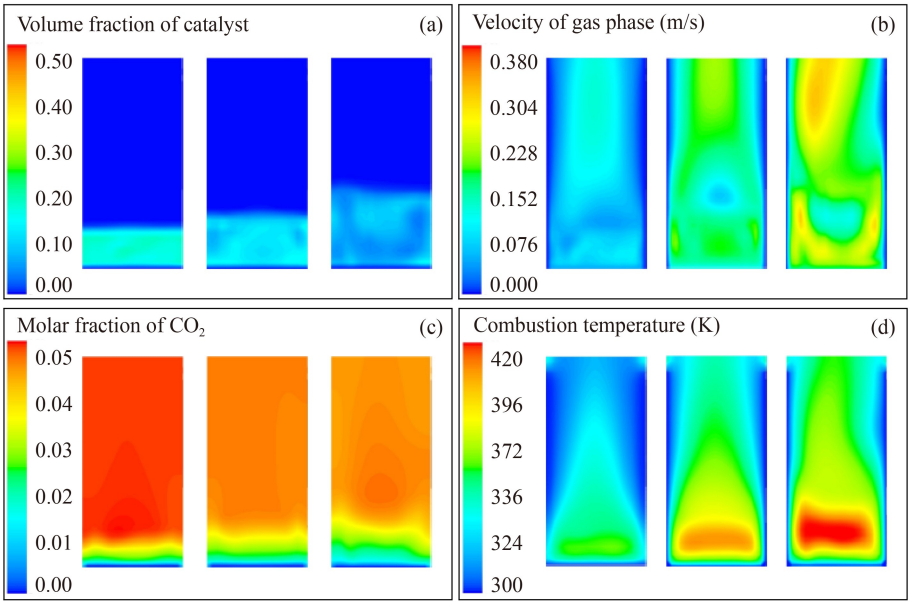

Fig. 10 Self-sustained catalytic combustion at the corresponding lean combustion limit conditions of 1000, 2000 and 3000 mL/min (from left to right): (a) particle volume fraction, (b) gas velocity, (c) CO_2 concentration and (d) combustion temperature distribution.

by H_2 temperature programmed reduction. XPS results also show that the presence of oxygen vacancies (Cu^+–[O_v]–Ce^{3+}) increases the adsorption and activation of CO, namely, the reaction between adsorbed CO and lattice oxygen, which follows the M-K mechanism. To simulate the combustion processes within the reactors, a CFD program is used coupled with a diffusion/kinetic-limited reaction model. Results suggest that the catalytic combustion in the fluidized state performs better (lower lean burn limit and wider elevated temperature zone) than that in the bubbling and fixed states. More importantly, when the CO in feed gas reaches a critical level, the self-sustained catalytic combustion of CO induced by the fluidized bed could trigger flame combustion, thus broadening the scope of purification of CO-containing exhaust gases.

Declaration of Competing Interest The authors declare that they have no known competing financial interests or personal relationships that could have appeared to influence the work reported in this paper.

Acknowledgements We gratefully acknowledge the financial support from the National Natural Science Foundation of China (No. 52176141).

References

Águila G, Gracia F, Araya P (2008). CuO and CeO_2 catalysts supported on Al_2O_3, ZrO_2, and SiO_2 in the oxidation of CO at low temperature. Applied Catalysis A, General, 343(1–2): 16–24

Avgouropoulos G, Ioannides T (2003). Selective CO oxidation over CuO–CeO_2 catalysts prepared via the urea–nitrate combustion method. Applied Catalysis A, General, 244(1): 155–167

Avgouropoulos G, Ioannides T, Matralis H (2005). Influence of the preparation method on the performance of CuO–CeO_2 catalysts for the selective oxidation of CO. Applied Catalysis B: Environmental, 56(1–2): 87–93

Benyahia S (1994). Synthesis gas formation by catalytic oxidation of methane fluidized bed reactors. Powder Technology, 146(1–2): 11–21

Bin F, Kang R, Wei X, Hao Q, Dou B (2019). Self-sustained combustion of carbon monoxide over $CuCe_{0.75}Zr_{0.25}O_\delta$ catalyst: stability operation and reaction mechanism. Proceedings of the Combustion Institute, 37(4): 5507–5515

Bin F, Wei X, Li B K S, Hui K S (2015). Self-sustained combustion of carbon monoxide promoted by the Cu–Ce/ZSM-5 catalyst in $CO/O_2/N_2$ atmosphere. Applied Catalysis B: Environmental, 162: 282–288

Bizon K (2016). Autothermicity, multiplicity, yield and selectivity of catalytic processes in a polytropic fluidized bed reactor. Chemical Engineering Journal, 288: 834–844

Chen A, Yu X, Zhou Y, Miao S, Li Y, Kuld S, Sehested J, Liu J, Aoki T, Hong S, et al. (2019). Structure of the catalytically active copper–ceria interfacial perimeter. Nature Catalysis, 2(4): 334–341

Chen Y, Liu D, Yang L, Meng M, Zhang J, Zheng L, Chu S, Hu T (2013). Ternary composite oxide catalysts CuO/Co_3O_4–CeO_2 with wide temperature-window for the preferential oxidation of CO in H_2-rich stream. Chemical Engineering Journal, 234: 88–98

Du P, Wang W, Jia C, Song Q, Huang Y, Si R (2016). Effect of strongly bound copper species in copper–ceria catalyst for preferential oxidation of carbon monoxide. Applied Catalysis A, General, 518: 87–101

Dubinin Y, Yazykov N, Reshetnikov S, Yakovlev V (2021). Catalytic combustion of sulfur-containing liquid fuels in the fluidized bed: experiment and modeling. Journal of Industrial and Engineering Chemistry, 93: 163–169

Duyar M, Ramachandran A, Wang C, Farrauto R (2015). Kinetics of CO_2 methanation over Ru/γ-Al_2O_3 and implications for renewable energy storage applications. Journal of CO_2 Utilization, 12: 27–33

Girimonte R, Formisani B (2009). The minimum bubbling velocity of fluidized beds operating at high temperature. Powder Technology, 189(1): 74–81

Goshima T, Yoshida Y, Shimazaki K, Fukudome K, Mizuta K, Nii S (2017). Experimental investigation on gas-solid behavior in fluidized beds with superfine particles. Chemical Engineering & Technology, 40(12): 2295–2304

Gu C, Qi R, Wei Y, Zhang X (2018). Preparation and performances of nanorod-like inverse CeO_2–CuO catalysts derived from Ce-1,3,5-Benzene tricarboxylic acid for CO preferential oxidation. Reaction Kinetics, Mechanisms and Catalysis, 124(2): 651–667

Hu C, Zhu Q, Jiang Z, Chen L, Wu R (2009). Catalytic combustion of dilute acetone over Cu-doped ceria catalysts. Chemical Engineering Journal, 152(2–3): 583–590

Iamarino M, Chirone R, Pirone R, Russo G, Salatino P (2002). Catalytic combustion of methane in a fluidized bed reactor under fuel-lean conditions. Combustion Science and Technology, 174(11–12): 361–375

Jia A, Hu G, Meng L, Xie Y, Lu J, Luo M (2012). CO oxidation over CuO/$Ce_{1-x}Cu_xO_{2-\delta}$ and $Ce_{1-x}Cu_xO_{2-\delta}$ catalysts: synergetic effects and kinetic study. Journal of Catalysis, 289: 199–209

Jia C, Dai Y, Yang Y, Chew J (2020). A fluidized-bed model for NiMgW-catalyzed CO_2 methanation. Particuology, 49: 55–64

Kang R, Ma P, He J, Li H, Bin F, Wei X, Dou B, Hui K, Hui K (2021). Transient behavior and reaction mechanism of CO catalytic ignition over a CuO–CeO_2 mixed oxide. Proceedings of the Combustion Institute, 38(4): 6493–6501

Kang R, Wei X, Ma P, Bin F, He J, Hao Q, Dou B (2020). Self-sustained combustion of CO with transient changes and reaction mechanism over $CuCe_{0.75}Zr_{0.25}O_\delta$ powder for honeycomb ceramic catalyst. Fuel, 263: 116637

Lazarovici A, Kalliadasis S, Merkin J, Scott S, Simon P (2004). The propagation and inhibition of an exothermic branched-chain flame with an endothermic reaction and radical scavenging. Journal of Engineering Mathematics, 49(1): 41–55

Li J, Yao X, Liu L, Zhong X, Lu C (2021). Heat transfer characterization and improvement in an external catalyst cooler fluidized bed. Particuology, 56: 103–112

Li J, Zhu Q, Peng W, Zhang Q, Luo G, Wei F (2017). Novel hierarchical Ni/MgO catalyst for highly efficient CO methanation in a fluidized bed reactor. AIChE Journal. American Institute of Chemical Engineers, 63(6): 2141–2152

Liang W, Li X, Ju H, Ren S (2022). Adsorption and dissociation mechanism of toluene on Pd (111) and PdO (101) surface: first principle calculation. Surface Science, 720: 122051

Liu B, Ji S (2013). Comparative study of fluidized-bed and fixed-bed reactor for syngas methanation over Ni–W/TiO_2–SiO_2 catalyst.

Journal of Energy Chemistry, 22(5): 740–746

Liu Q, Chen R, Zeng M, Fei Z, Chen X, Zhang Z, Tang J, Cui M, Qiao X (2020a). High-efficiency treatment of benzaldehyde residue using two-stage fluidized-bed/fixed-bed catalytic system. Environmental Technology, 41(22): 2898–2906

Liu X, Xu G, Gao S (2008). Micro fluidized beds: wall effect and operability. Chemical Engineering Journal, 137(2): 302–307

Liu Y, Mao D, Yu J, Zheng Y, Guo X (2020b). Facile preparation of highly active and stable CuO–CeO_2 catalysts for low-temperature CO oxidation via a direct solvothermal method. Catalysis Science & Technology, 10(24): 8383–8395

Luo M, Fang P, He M, Xie Y (2005). In situ XRD, Raman, and TPR studies of CuO/Al_2O_3 catalysts for CO oxidation. Journal of Molecular Catalysis A,Chemical, 239(1–2): 243–248

Meng F, Xia Y, Zhang J, Qiu D, Chu Y, Tang Y (2021). Cu/Cr co-stabilization mechanisms in a simulated Al_2O_3–Fe_2O_3–Cr_2O_3–CuO waste system. Frontiers of Environmental Science & Engineering, 15(6): 116

Nam H, Kim J, Kim H, Kim M, Jeon S, Jin G, Won Y, Hwang B, Lee S, Baek J, et al. (2021). CO_2 methanation in a bench-scale bubbling fluidized bed reactor using Ni-based catalyst and its exothermic heat transfer analysis. Energy, 214: 118895

Paasikallio V, Kalogiannis K, Lappas A, Lehto J, Lehtonen J (2017). Catalytic fast pyrolysis: influencing bio-oil quality with the catalyst-to-biomass ratio. Energy Technology (Weinheim), 5(1): 94–103

Parmon V, Simonov A, Sadykov V, Tikhov S (2015). Catalytic combustion: achievements and problems. Combustion, Explosion, and Shock Waves, 51(2): 143–150

Rau J, Chen J, Lin M, Wey M (2010). Removal the coal ash, NO, and SO_2 simultaneously by the fluidized-bed catalyst reactor. Energy & Fuels, 24(3): 1711–1719

Talluri B, Yoo K, Kim J (2022). *In situ* growth of self-composed cerium iron oxide hierarchal structures as a novel anode electrocatalyst for direct methanol fuel cells. Ceramics International, 48(3): 3628–3635

Wang F, Fu R, Hu R, Ding R (2013). Reactors used for catalytic combustion of methane. Advanced Materials Research, 634–638: 798–804

Wang Z, Li R, Chen Q (2015). Enhanced activity of CuCeO catalysts for CO oxidation: influence of Cu_2O and the dispersion of Cu_2O, CuO, and CeO_2. Chemphyschem: a European Journal of Chemical Physics and Physical Chemistry, 16(11): 2415–2423

Wang X, Jin Y, Chen W, Zou R, Xie J, Tang Y, Li X, Li L (2021). Electro-catalytic activity of CeO_x modified graphite felt for carbamazepine degradation via E-peroxone process. Frontiers of Environmental Science & Engineering, 15(6): 122

Yang Z, Yang P, Zhang L, Guo M, Yan Y (2014). Investigation of low concentration methane combustion in a fluidized bed with Pd/Al_2O_3 as catalytic particles. RSC Advances, 4(103): 59418–59426

Zeng S, Zhang W, Liu N, Su H (2013). Inverse CeO_2/CuO catalysts prepared by hydrothermal method for preferential CO oxidation. Catalysis Letters, 143(10): 1018–1024

Zhang X, Zhang X, Song L, Hou F, Yang Y, Wang Y, Liu N (2018). Enhanced catalytic performance for CO oxidation and preferential CO oxidation over CuO/CeO_2 catalysts synthesized from metal organic framework: effects of preparation methods. International Journal of Hydrogen Energy, 43(39): 18279–18288

Zhao C, Hao Q, Zhang Q, Yan N, Liu J, Dou B, Bin F (2019). Catalytic self-sustained combustion of toluene and reaction pathway over $Cu_xMn_{1-x}Ce_{0.75}Zr_{0.25}/TiO_2$ catalysts. Applied Catalysis A, General, 569: 66–74

Zou H, Dong X, Lin W (2006). Selective CO oxidation in hydrogen-rich gas over CuO/CeO_2 catalysts. Applied Surface Science, 253(5): 2893–2898

Żukowski W, Berkowicz G (2019a). The combustion of liquids and low-density solids in a cenospheric fluidized bed. Combustion and Flame, 206: 476–489

Żukowski W, Berkowicz G (2019b). The combustion of polyolefins in inert and catalytic fluidised beds. Journal of Cleaner Production, 236: 117663